PROCEEDINGS, 48th Workshop on Geothermal Reservoir Engineering
Stanford University, Stanford, California, February 6-8, 2023
SGP-TR-224

Seismotectonic Evolution and Geothermal Energy Production in the Salton Sea Geothermal Field

Malcolm C. A. White[1*], Nori Nakata[1,2], Verónica Rodríguez Tribaldos[3], Avinash Nayak[2] and Patrick F. Dobson[2]

[1]Massachusetts Institute of Technology, Cambridge, MA, USA

[2]Lawrence Berkeley National Laboratory, Berkeley, CA, USA

[3]GFZ German Research Centre for Geosciences, Potsdam, Germany

[*]malcolmw@mit.edu

Keywords: Induced seismicity, seismicity-rate hindcasting, Salton Sea Geothermal Field

ABSTRACT

Geothermal brines in the Salton Sea Geothermal Field (SSGF), Southern California, offer abundant geothermal energy and significant amounts of dissolved lithium, both of which can be harvested to support the ongoing clean-energy transition. Harvesting these resources, however, could induce earthquakes in the seismically active Brawley Seismic Zone. To support responsible development of SSGF resources, we retrospectively correlate 50 years of seismic history in the SSGF (1972-2022) with 40 years of contemporaneous geothermal power plant operations (1982-2022). We conclude that the background seismicity rate in the SSGF is directly proportional to production and injection rates at geothermal wells during the period 1982-1996, and that this proportionality relationship weakens between 1996 and 2005, and nearly vanishes after 2005. After 2005, the background seismicity rate remains elevated above the pre-production rate; however, production and injection rates offer marginally more predictive power than assuming a simple constant background seismicity rate. These observations motivate development of more sophisticated models for understanding the relationship between geothermal power plant activity and seismicity in the region. We hypothesize that the Brawley Fault may act as a hydraulic barrier inhibiting fluid migration between the eastern and western portions of the field, thus imposing first-order constraint on the field's overall geomechanical response to plant activity. We suggest that refined modeling efforts take this structural constraint into consideration.

INTRODUCTION

The Salton Sea Geothermal Field (the target of this study) sits on the southern shore of the Salton Sea, within the Brawley Seismic Zone (BSZ)—a diffuse zone of seismicity connecting the Imperial Fault to the south and the Southern San Andreas Fault to the north with a roughly NNW trend. The BSZ manifests the transtensional tectonic regime of the transition zone between the divergent East Pacific Rise and the transform boundary between the Pacific and North American Plates. Earthquakes in the BSZ generally shallow along strike towards the NNW, and seismic activity nearly ceases where the Brawley Fault meets the Southern San Andreas Fault near Bombay Beach (Figure 1). The SSGF coincides with a cloud of seismicity trending orthogonally to the Brawley Fault.

The SSGF occupies a ~6 km wide pull-apart basin within the transtensional regime of the BSZ, the spreading axis of which trends roughly NE/SW (Kaspereit et al., 2016), parallel to the trend of the cloud of seismicity mentioned above. Crustal thinning throughout the Salton Trough enables the upward migration of mantle-derived magma, which drives circulation of geothermal brine in shallow (~2-4 km depth), permeable sediments in the SSGF. These permeable sediments overlay metamorphosed sediments on top of the igneous basement (Han et al., 2016).

The first commercial geothermal power plant began generating electricity using steam derived from geothermal brines in the SSGF in 1982 (Anderson, 1983). Eleven plants continue operating today. The current field power production is ~400 MW (345 MW for the 10 BHER plants and 55 MW for the Featherstone plant), with expansion of the field planned. Kaspereit et al. (2016) estimated the resource potential of the field to be 2950 MW. In addition to abundant thermal energy, geothermal brines in the SSGF also contain significant amounts of dissolved lithium—an increasingly valuable metal used to store energy. Investigation is ongoing as to whether lithium can be economically and sustainably recovered from the geothermal brine that is already being extracted from the subsurface to generate electricity. With the increasing urgency to transition to carbon-free energy sources, and the associated demand for efficient energy stores, such as lithium-ion batteries, the SSGF is a target-rich environment, and development of these resources is likely to accelerate in the near future.

Although resources in the SSGF hold significant potential for fueling the clean-energy transition, development must be carried out responsibly. Extracting and injecting geofluids perturbs the subsurface stress regime and is liable to activate pre-existing faults. In this paper, we seek to inform responsible development of SSGF resources by investigating the relationship between geothermal plant operations and seismic activity in the SSGF. We analyze 50 years of earthquake data in relation to contemporaneous geothermal plant operations, including 10 years prior to any commercial activity. We conclude that the rate of earthquake occurrences is proportional to the production and injection rates at geothermal wells during the first fourteen years of plant operations (1982-1996). The fidelity of this relationship wanes over the subsequent 9 years (1996-2005), and is virtually non-existent after 2005—more sophisticated models than those developed in this paper are needed to model any causal relationships between plant operations and seismic activity. To this end, we

hypothesize that the main through-going fault (the Brawley Fault) acts as a hydraulic barrier separating the eastern and western portions of the field, and suggest that development of models incorporating the effect of this structural constraint may be a fruitful direction for further research.

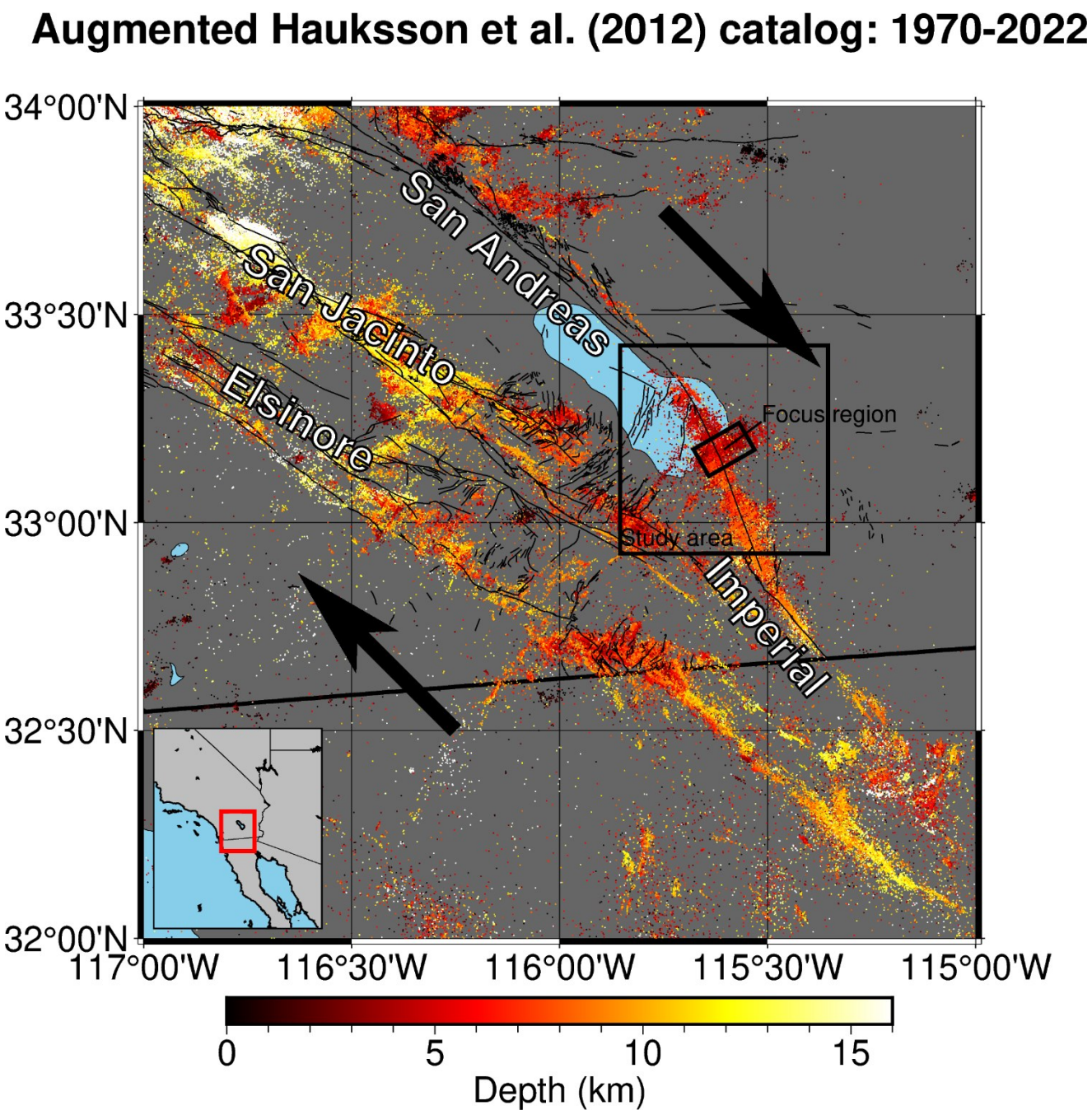

Figure 1: Regional context of our study area and focus region. Dots represent locations of earthquakes in the Augmented Hauksson et al. (2012) catalog between 1970 and 2022, color-coded by hypocenter depth. Large black arrows show nominal relative motions of the Pacific (NW) and North American (SE) tectonic plates.

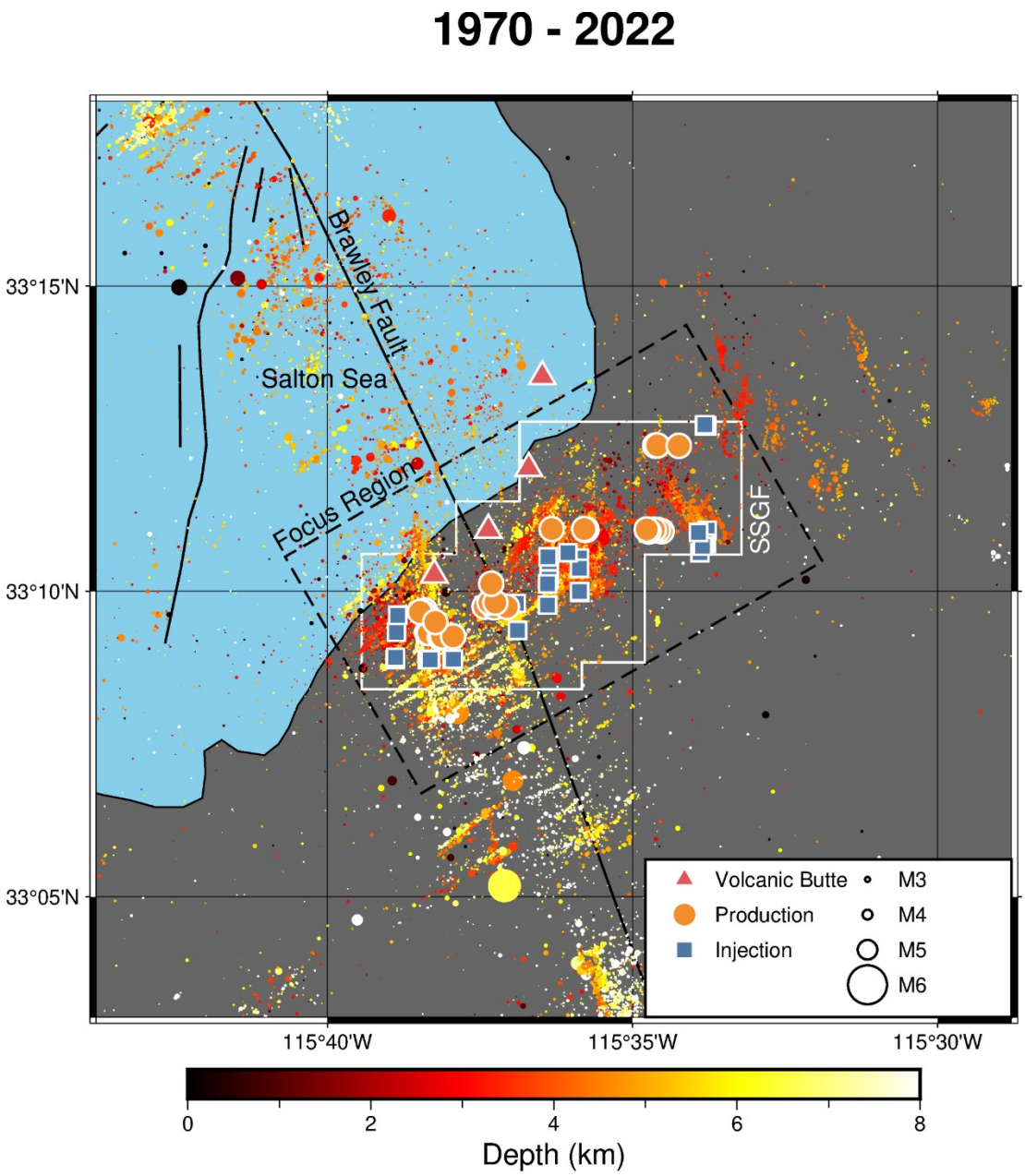

Figure 2: Local overview of our study area (mapped area) and focus region (rotated, black, dashed rectangle). Orange circles and blue squares with white edges represent the locations of all currently active production and injection wells in our study area, respectively. Other circles represent seismicity between 1970 and 2022 from the Augmented Hauksson et al. (2012) catalog, color-coded by depth and scaled according the magnitude. Red triangles represent the location of Holocene volcanic rhyolite domes. The polygon delineated by the solid, white line represents the Salton Sea Geothermal Field (as specified by the California Department of Conservation, Division of Oil, Gas, and Geothermal Resources). Solid black lines represent known Quaternary fault traces.

2. RESULTS

2.1 Earthquake Catalog Data

We analyze 50 years of earthquake data from the combined SCSN standard catalog (1972-1981) (Hutton et al., 2010) and the high-precision, waveform-relocated catalog of Hauksson et al. (2012) (1981-2022). We determine that the catalog considered is at least 95% complete at M=2.34 (Figure 3a) within our study area (Figures 1 and 2) throughout the entire period analyzed, and thus restrict our analysis to M≥2.34 earthquakes.

2.2 Geothermal Plant Operations Data

The California Department of Conservation (CDC) mandates that geothermal plant operators report on plant operations each month. These reports comprise measurements such as gross fluid produced, gross fluid injected, average fluid temperature (injected/produced), and average fluid pressure (injected/produced). The CDC makes these monthly values publicly available on a per-well basis, which we download via the GeoSteam application for this study (Figure 3b).

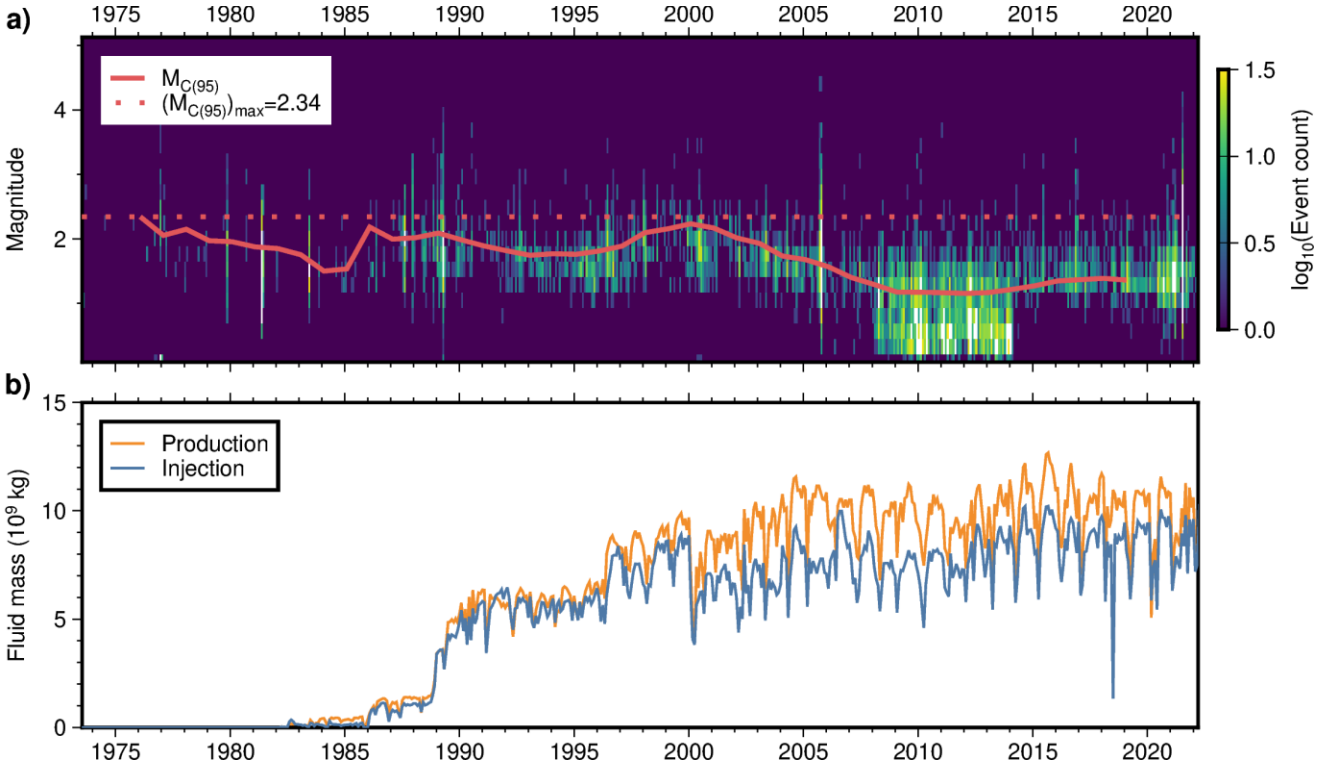

Figure 3: Panel (a) shows the frequency-magnitude distribution as a function of time (background color), magnitude of 95% completeness $M_{C(95)}$ computed using a five-year rolling window (solid red curve), and maximum value of $M_{C(95)}$ (dotted red line). Panel (b) shows the production and injection histories.

2.3 Looking Back at Seismicity

In addition to the clustering of shallow earthquakes near geothermal wells (Figure 2), the number of background earthquakes (i.e., excluding foreshocks and aftershocks) observed within the SSGF increased significantly during the first ten years of geothermal energy production (1982-1992), relative to the ten years prior (1972-1982) (Figure 4). In an effort to model the relationship between geothermal plant operations and the occurrences of earthquakes in the SSGF, Brodsky and Lajoie (2013) proposed the following simple linear-regression model for retrospectively modeling (hindcasting) background seismicity rates as a function of injection and production rates:

$$\hat{\mu}(t) = \begin{cases} \beta_0 P(t) + \gamma_0 I(t) & t_0 \le t < t_1 \\ \beta_1 P(t) + \gamma_0 I(t) & t_1 \le t < t_2 \\ \vdots & \vdots \\ \beta_n P(t) + \gamma_n I(t) & t_n \le t < t_{n+1}, \end{cases} \quad (1)$$

in which $\hat{\mu}$ is the hindcasted background seismicity rate (earthquakes per unit time, excluding foreshocks and aftershocks); t is time; β_i, and γ_i are regression coefficients determined using ordinary least-squares regression on six years of data; P and I are production and injection rates, respectively; and $t_k = t_0 + k\Delta t$ for integer k and Δt equal to six months. Such a model comprises four regression coefficients per year, and would thus require 160 parameters to model the entire 40-year history of the geothermal field we analyze. Brodsky and Lajoie (2013) concluded that their model provided meaningful insights into the causal relationship between well operations and the earthquake occurrence rate.

In this paper, we simplify the model of Brodsky and Lajoie (2013) by reducing the number of free parameters used to hindcast seismicity rates. We conclude that seismicity rates can indeed be hindcast as a function of production and injection at geothermal wells; however, the fidelity of our simplified hindcasting model varies significantly throughout the analyzed period (Figure 5). We correlate these variations with changes in well operations.

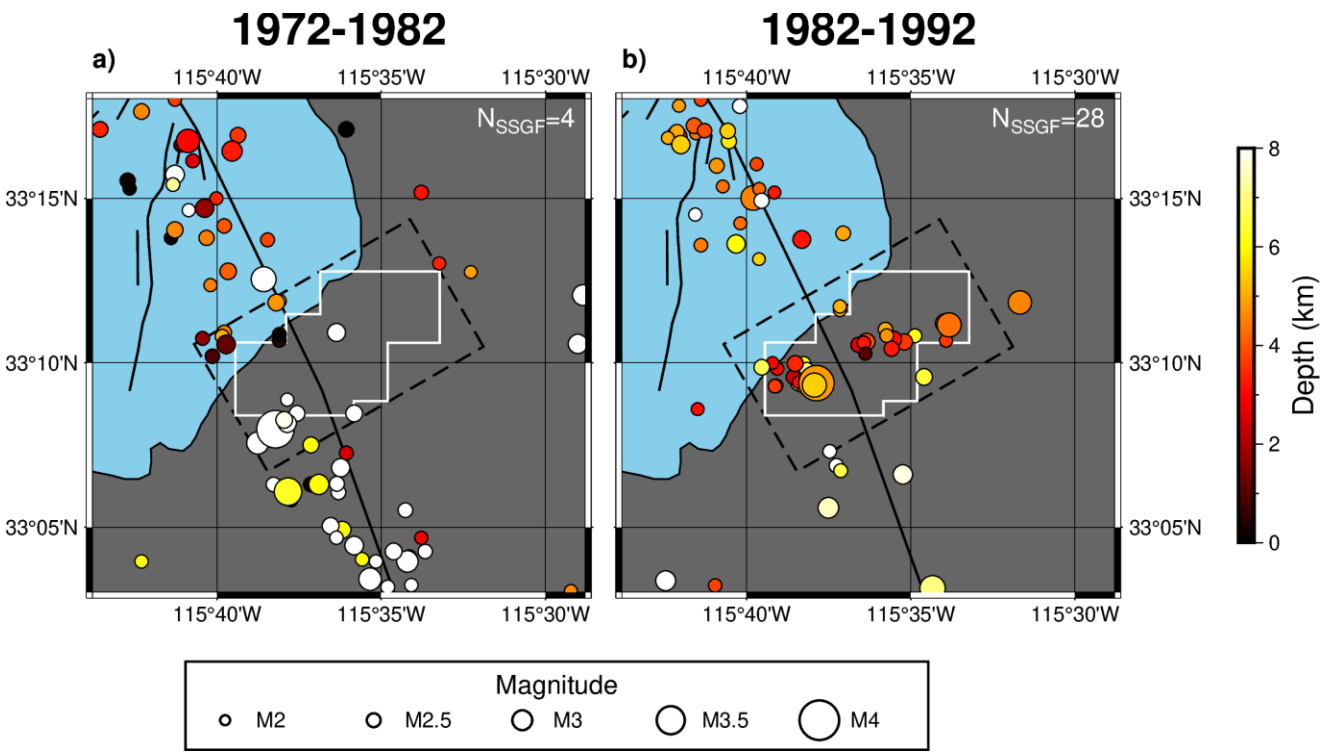

Figure 4: Shows background seismicity within our study area as circles, color-coded by hypocenter depth, during (a) the ten years prior to the beginning of geothermal energy production (1972-1982) and (b) the ten following years (1982-1992). N_{SSGF} represents the number of background events (averaged over 128 declustered catalogs) within the Salton Sea Geothermal Field (white polygon). White circles represent events with hypocenter depth ≥ 8 km.

Mainshock-aftershock sequences alter the occurrence rate of earthquakes orders-of-magnitude more than any external physical controls (e.g., geothermal plant operations). The background seismicity rate, however, is insensitive to intense aftershock sequences and reveals subtler variations, such as those potentially caused by geothermal plant operations. The background seismicity rate is thus often preferred when investigating the relationships between physical controls and earthquake occurrences (e.g., Brodsky and Lajoie, 2013; Martínez-Garzón et al., 2018; Trugman et al., 2016). We estimate the background seismicity rate using two independent methods (Figure 5). The first approach follows that of Brodsky and Lajoie (2013) based on the Epidemic Type Aftershock Sequence (ETAS) model (Ogata, 1988). The second approach uses declustered catalogs obtained via the Nearest-Neighbor Distance (NND) algorithm of Zaliapin and Ben-Zion (2020). In the following analysis, we consider only the trend of the seismicity-rate histories, which we obtain by decomposing each history into (1) seasonal, (2) trend, and (3) residual components with the Seasonal-Trend decomposition using LOESS (STL) algorithm (Cleveland et al., 1990). The seismicity-rate histories from these independent methods agree well (coefficient of determination $R^2 = 0.92$).

We assume a model of the form

$$\hat{\mu}(t) = \begin{cases} \alpha_0 + \beta_0 P(t) + \gamma_0 I(t) & t_0 \le t < t_1 \\ \alpha_1 + \beta_1 P(t) + \gamma_0 I(t) & t_1 \le t < t_2 \\ \vdots & \vdots \\ \alpha_n + \beta_n P(t) + \gamma_n I(t) & t_n \le t < t_{n+1}, \end{cases} \tag{2}$$

in which we have added a constant term α_i to the model expressed by Equation (1) and allow t_k to take on arbitrary values. A cumulative sum of residuals (CUSUM) test (Brown et al., 1975) indicates that a statistically significant change (at the 95% confidence level) in regression coefficients occurs in 1996. This change point coincides with the beginning of a period of time (1996-2005) during which the average temperature of fluid being injected into the subsurface fluctuated significantly around the relatively stable temperature during the preceding period (Figure 6). Furthermore, the apparatus used to monitor fluid production and injection rates changed circa 2005/2006 (Emily Brodsky; personal communication). We thus divide the 40-year history of geothermal energy operations into (1) "early" (1982-1996), (2) "intermediate" (1996-2006), (3) and "late" (2006-present) time periods, and build a hindcasting model of the form

$$\hat{\mu}(t) = \begin{cases} \alpha_0 + \beta_0 P(t) + \gamma_0 I(t) & 1982 \le t < 1996 \\ \alpha_1 + \beta_1 P(t) + \gamma_1 I(t) & 1996 \le t < 2006 \\ \alpha_2 + \beta_2 P(t) + \gamma_2 I(t) & 2006 \le t \end{cases} \tag{3}$$

We determine two separate hindcasting models by fitting Equation (3) via OLS regression to seismicity rate histories obtained by each of the two methods described above (i.e., the ETAS and NND methods).

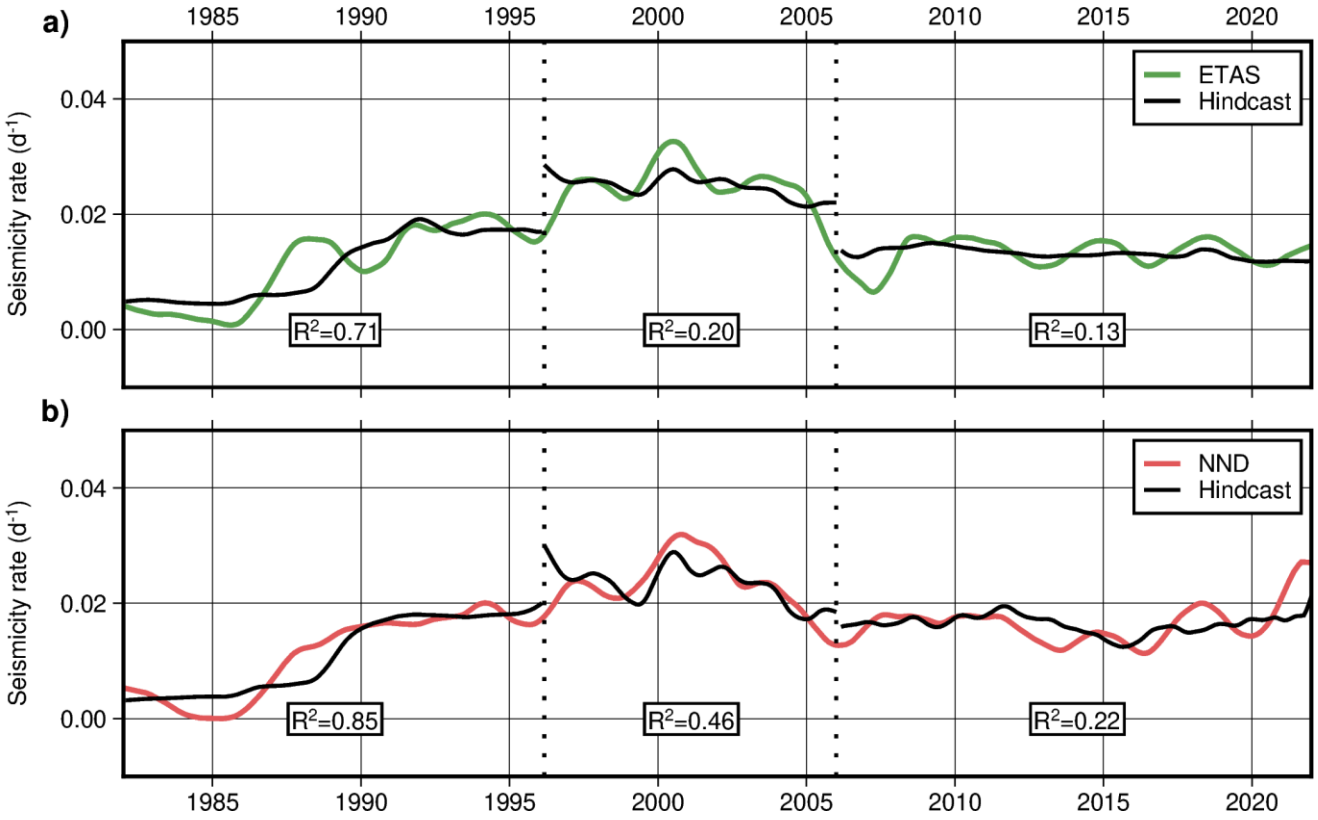

Figure 5: Shows the background seismicity rate estimated from the Augmented Hauksson et al. (2012) catalog using (a) the ETAS model and (b) declustered catalogs. Solid black curves show the piecewise-linear hindcast model. Dotted, black lines represent discontinuities in the hindcast models. R^2 values quantify the correlation between the observed seismicity rate and hindcast model for each time period.

Hindcasting fidelity between 1982 and 1996 can be described as moderate to strong (R^2 values of 0.71 and 0.85 for ETAS and NND results, respectively). During the first fourteen years of energy production, background seismicity rates appear to be directly proportional to production and injection rates.

Hindcasting fidelity during the next ten years (1996-2006) can be described as weak to moderate (R^2 values of 0.20 and 0.48 for ETAS and NND results, respectively). This period coincides with significant fluctuations in the average temperature of injected fluids.

Hindcasting fidelity after 2006 is weak. Models based on injection and production histories during this period provide marginally more explanatory power than simply assuming a constant background seismicity rate. The background seismicity rate remains elevated during this period, despite the lack of a simple relationship to geothermal plant activity. These results motivate the development of more sophisticated models.

3. DISCUSSION

Although the model proposed by Brodsky and Lajoie (2013) expresses a simple linear relationship between plant operations and background seismicity, it has a large number of free parameters—one free parameter for every three data points. Such a piecewise model can fit the data arbitrarily well by fitting a sufficiently large number of pieces to sufficiently small subsets of data. Speaking philosophically, the interpretability of a physical model is inversely proportional to the number of free parameters it comprises. We have shown that many of these parameters can be effectively eliminated, particularly during the first fourteen years of energy production: Whereas Brodsky and Lajoie's (2013) model comprises 56 free parameters during this period, ours maintains much of the explanatory power using only three free parameters. By fixing our model discontinuities to coincide with known changes in plant operations, we have made it easier to interpret. We interpret our model results as follows:

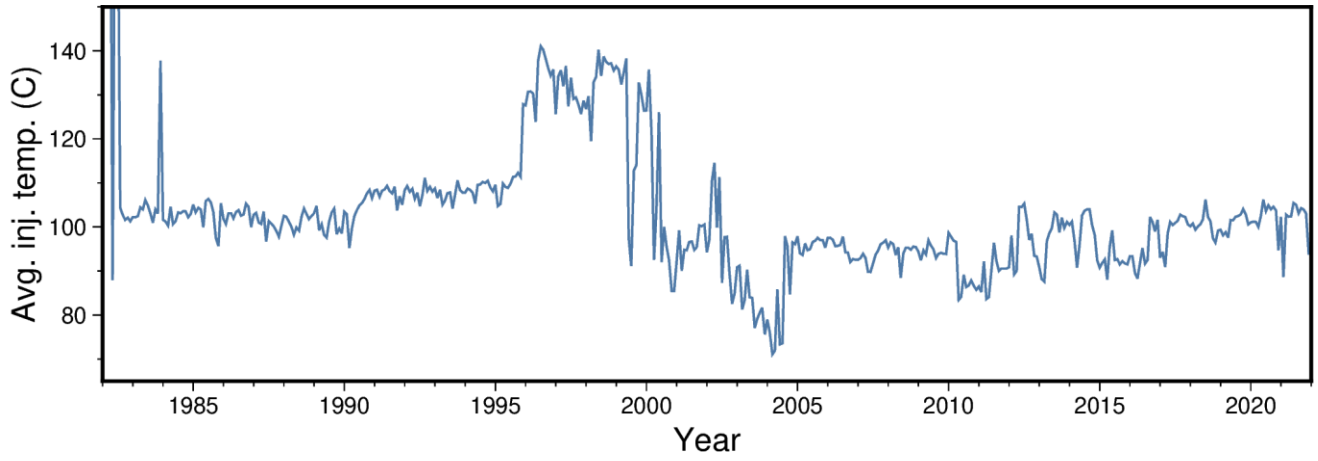

Figure 6: Shows the weighted (by fluid mass) average temperature of injected brine.

Prior to geothermal plant operations, we consider the reservoir and surrounding crust as existing in a steady state within the ambient tectonic stress regime, with a pre-existing network of faults related to basin extension randomly distributed throughout. Pre-production failure of secondary faults is minimal, as the majority of tectonic stress is accommodated by failure on the Brawley Fault and aseismic creep (Lohman and McGuire, 2007). As geothermal plant activity increased, pore-pressure perturbations propagated away from the injection well flow intervals (i.e., permeable zones in the injection wells between the casing shoe and the bottom of the well) causing many pre-existing faults to become critically stressed and fail. A roughly proportional increase in the background seismicity rate accompanied fluid production and injection, and the number of nearly critical pre-existing faults thus decreased with increasing time. The seismogenic response of the crust to well activity was strongest early in the history of plant operations. By the early nineties, plant operations and the background seismicity rate both stabilized. Failure was induced on pre-existing faults at a relatively steady rate as fluids moved through the subsurface at a relatively steady rate.

The average temperature of injected brine increased from 105.0 °C (standard deviation 4.4 °C) between 1985 and 1996 to 132.8 °C (standard deviation 5.1 °C) between 1996 and 1999 (Figure 6). The average temperature fluctuated between 1999 and 2005 before stabilizing at 96.5 °C (standard deviation 5.2 °C) after 2005. Pore-pressure perturbations during the period between 1996 and 2005 were thus influenced by both fluid transfer rates and fluctuating fluid temperatures. Interpreting induced failure as a simple function of a homogeneous diffusion process is insufficient during this period, and the relationship of proportionality between background seismicity rate and fluid transfer rates weakens.

Injection temperatures stabilized after 2005, and although plant activity remained high, the number of nearly critical pre-existing faults was substantially lower than earlier in production history. Heterogeneity of Earth structure and the induced stress field predominantly controlled the rate of induced earthquakes during this period, and the rate of fluid transfer offers marginally more insight into the rate of induced earthquakes than simply assuming a constant rate.

In this paper, we model the geomechanical response of the crust to production and injection at geothermal wells, averaged over the entire SSGF—no spatial dependence is incorporated into our model. The termination of seismic lineations at the Brawley Fault, however, suggests that it constitutes a significant structural barrier. Furthermore, low-permeability fault gouge is likely associated with the Brawley Fault (Morrow et al., 1984; Ikari et al., 2009). Both of these features suggest that the Brawley Fault may act as a hydraulic barrier inhibiting fluid flow between the eastern and western portions of the field. We thus suggest that further modeling efforts account for this major structural constraint. We also suggest incorporating the effect of fluid injection temperature.

4. CONCLUSIONS

We analyzed 40 years (1982-2022) of geothermal plant operations in relation to 50 years (1972-2022) of earthquake history, including 10 years prior to plant operations, in the Salton Sea Geothermal Field. We developed a simple model for hindcasting background seismicity rates as a function of the production and injection rates of geothermal brine. We conclude from our hindcasting model that background seismicity is (1) moderately to strongly correlated with injection and production between 1982 and 1996, (2) weakly to moderately correlated between 1996 and 2005, and (3) weakly correlated after 2005. We interpreted these results within the context of a conceptual model incorporating elements of the seismotectonic evolution of and geothermal plant operations in the SSGF. These results will help inform the continued, safe development of geothermal and related resources in the SSGF. We hypothesize that the Brawley Fault acts as a major hydraulic barrier and suggest that future work account for this potential constraint on crustal response to geothermal plant operations.

APPENDIX A

A.1 Estimating Magnitude of Catalog Completeness M_C

The frequency-magnitude distribution of an incomplete catalog can be modeled using an exponentially modified Gaussian probability density function (White et al. 2019):

$$f(m;\ \mu,\sigma,\beta) = \beta \exp\left(\frac{\beta}{2}(2\mu+\beta\sigma^2)\right)\exp(-\beta m)\ \Phi\left(\frac{m-(\mu+\beta\sigma^2)}{\sigma}\right) \quad (5)$$

in which $\beta\exp(-\beta m)$ is an exponential distribution with decay rate β, which represents classical Gutenberg-Richter statistics for a complete catalog; $\Phi\left(\frac{m-(\mu+\beta\sigma^2)}{\sigma}\right)$ is a Gaussian CDF with mean $(\mu+\beta\sigma^2)$ and standard deviation σ, which represents a "thinning operator""; and $\exp\left(\frac{\beta}{2}(2\mu+\beta\sigma^2)\right)$is a normalization constant. The thinning operator represents the proportion of earthquakes of a given magnitude that are registered in an incomplete catalog. We define the level of catalog completeness $M_C = M_{C(95)}$ such that $\Phi\left(M_{C(95)}\right) = 0.95$. This implies that 95% of events that occur with $M = M_{C(95)}$ are registered in the catalog. We compute $M_{C(95)}$ using a five-year rolling window and take the maximum resulting value of the level of completeness for our analysis M_C.

A.2 Estimating Background Seismicity Rate with the ETAS Model

Let

$$\mathcal{H}_{1,2} \stackrel{\text{def}}{=} \{(t_i, M_i) | \tau_1 \le t_i < \tau_2\} \quad (6)$$

be the history of earthquake occurrences between times τ_1 and τ_2 in which (t_i, M_i) represents the time and magnitude, respectively, of the i^{th} earthquake. Then the ETAS model for the occurrence of earthquakes with magnitude greater than some threshold M_C is given by an inhomogeneous point process with "conditional intensity factor" $\lambda_\theta\left(t|\ \mathcal{H}_{1,2}\right)$ at time t given history $\mathcal{H}_{1,2}$:

$$\lambda_\theta\left(t|\mathcal{H}_{1,2}\right) \stackrel{\text{def}}{=} \mu + \sum_{i|t_i<t} \frac{K}{(t-t_i+c)^p} 10^{\alpha(M_i-M_C)} \quad (7)$$

for $\tau_1 \le t < \tau_2$, in which $\theta \stackrel{\text{def}}{=} \langle \mu, K, c, \alpha, p \rangle$ is the vector of free parameters μ, K, c, α, and p. μ, our parameter of interest, represents the background seismicity rate, K represents the productivity of aftershock sequences, c and p represent the temporal decay of aftershock sequences, and α represents Gutenberg-Richter statistics.

In this work, we follow Brodsky and Lajoie (2013) by fixing $\alpha = 1$, $c = 0.006$ *d*, and $M_C = 2.34$ (Brodsky and Lajoie (2013) used $M_C = 1.75$), and inverting for the three remaining parameters μ, K, and p using the maximum-likelihood method in two-year rolling windows.

A.3 Estimating Background Seismicity Rate with Declustered Catalogs

We compute the normalized nearest-neighbor proximity α_i for each event (indexed by i) in the catalog following Zaliapin and Ben-Zion (2020). We then decluster the catalog by stochastically discarding events with probability $P_i = \min(\alpha_i A_0, 1)$ in which we set the inverse threshold $A_0 = 10$. We then estimate the background seismicity rate by computing the average number of events per unit time in a two-year sliding window. Because the declustering procedure is stochastic, we report the background seismicity rate averaged over 128 declustered catalogs in Figures 4 and 5.

A.4 Decomposing Signals into Seasonal, Trend, and Residual Components

The production and injection histories show strong seasonal dependence as energy demands cycle annually. Because our background seismicity rates are computed in a two-year rolling window, we want to remove high-frequency fluctuations that are significantly shorter than this length of time. We decompose production, injection, and background seismicity rate histories into secular trend, seasonal, and residual components using Seasonal-Trend LOESS (Cleveland et al., 1990) (Figure 7).

ACKNOWLEDGMENTS

This work is supported by the U.S. Department of Energy, Office of Energy Efficiency and Renewable Energy (EERE), Geothermal Technologies Office, under Award Number DE-AC02–05CH11231 with Lawrence Berkeley National Laboratory.

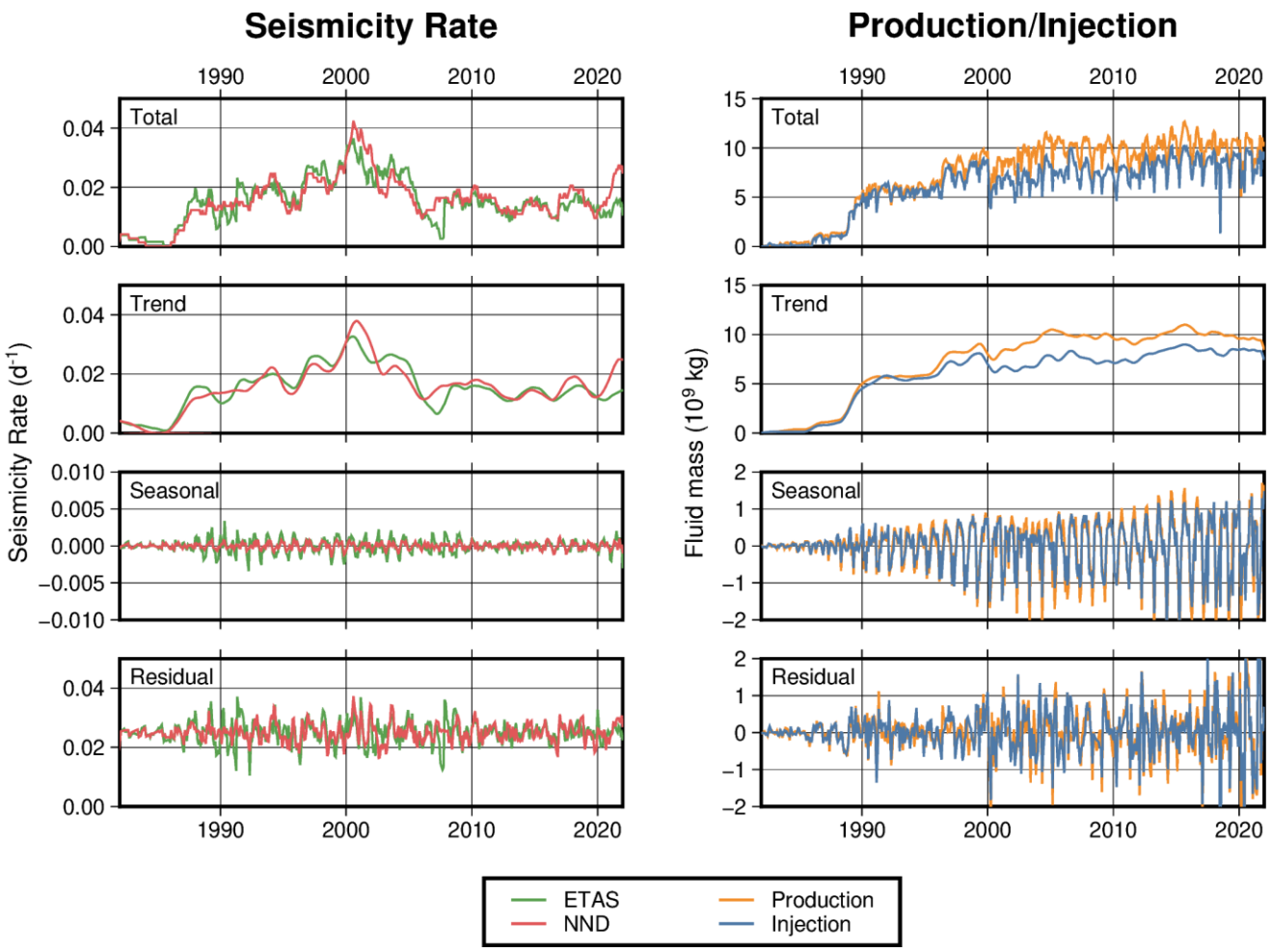

Figure 7: Shows the observed (a) seismicity rate and (e) production/injection histories. Panels (b) and (f) show the secular trend of the observed histories. Panels (c) and (g) show the seasonal component of the observed histories. Panels (d) and (h) show the residual component of the observed histories.

REFERENCES

Anderson, D.N.: Crystallizer clarifier process spells success for first Salton Sea project, Geothermal Resources Council Bulletin, March 1983, (1983), 14–15.

Brodsky, E.E., and Lajoie, L.J.: Anthropogenic Seismicity Rates and Operational Parameters at the Salton Sea Geothermal Field, Science, 341, (2013), 543–546, doi:10.1126/science.1239213.

Brown, R.L., Durbin, J., and Evans, J.M.: Techniques for Testing the Constancy of Regression Relationships Over Time, Journal of the Royal Statistical Society: Series B (Methodological), 37, (1975), 149–163, doi:10.1111/j.2517-6161.1975.tb01532.x.

Cleveland, R.B., Cleveland, W.S., McRae, J.E., and Terpenning, I.: STL: A Seasonal-Trend Decomposition Procedure Based on Loess, Journal of Official Statistics, 6, (1990), 3–73.

Han, L., Hole, J.A., Stock, J.M., Fuis, G.S., Kell, A., Driscoll, N.W., Kent, G.M., Harding, A.J., Rymer, M.J., González-Fernández, A., and Lázaro-Mancilla, O.: Continental rupture and the creation of new crust in the Salton Trough rift, Southern California and northern Mexico: Results from the Salton Seismic Imaging Project, Journal of Geophysical Research: Solid Earth, 121, (2016), 7469–7489, doi:10.1002/2016jb013139.

Hauksson, E., Stock, J.M., and Husker, A.L.: Seismicity in a weak crust: the transtensional tectonics of the Brawley Seismic Zone section of the Pacific–North America Plate Boundary in Southern California, USA, Geophysical Journal International, 231, (2022), 717–735, doi:10.1093/gji/ggac205.

Hauksson, E., Yang, W., and Shearer, P.M.: Waveform Relocated Earthquake Catalog for Southern California (1981 to June 2011) Short Note, Bulletin of the Seismological Society of America, 102, (2012), 2239–2244, doi:10.1785/0120120010.

Hutton, K., Woessner, J., and Hauksson, E.: Earthquake Monitoring in Southern California for Seventy-Seven Years (1932–2008), Bulletin of the Seismological Society of America, 100, (2010), 423–446, doi:10.1785/0120090130.

Ikari, M.J., Saffer, D.M., and Marone, C.: Frictional and hydrologic properties of clay-rich fault gouge, Journal of Geophysical Research: Solid Earth, 114, (2009), doi:10.1029/2008jb006089.

Kaspereit, D., Mann, M., Sanyal, S., Rickard, B., Osborn, W., and Hulen, J.: Updated conceptual model and reserve estimate for the Salton Sea geothermal field, Imperial Valley, California, Geothermal Resources Council Transactions, 40, (2016), 57–66.

Lohman, R.B., and McGuire, J.J.: Earthquake swarms driven by aseismic creep in the Salton Trough, California: Journal of Geophysical Research: Solid Earth, 112(B4), (2007), B04405, doi:10.1029/2006jb004596.

Martínez-Garzón, P., Zaliapin, I., Ben-Zion, Y., Kwiatek, G., and Bohnhoff, M.: Comparative Study of Earthquake Clustering in Relation to Hydraulic Activities at Geothermal Fields in California, Journal of Geophysical Research: Solid Earth, 123, (2018), 4041–4062, doi:10.1029/2017jb014972.

Morrow, C.A., Shi, L.Q., and Byerlee, J.D.: Permeability of fault gouge under confining pressure and shear stress, Journal of Geophysical Research: Solid Earth, 89, (1984), 3193–3200, doi:10.1029/jb089ib05p03193.

Ogata, Y.: Statistical Models for Earthquake Occurrences and Residual Analysis for Point Processes, Journal of the American Statistical Association, 83:401, (1988), 9–27, doi: 10.1080/01621459.1988.10478560

Trugman, D.T., Shearer, P.M., Borsa, A.A., and Fialko, Y.: A comparison of long-term changes in seismicity at The Geysers, Salton Sea, and Coso geothermal fields, Journal of Geophysical Research: Solid Earth, 121, (2016), 225–247, doi:10.1002/2015jb012510.

van der Elst, N.J., Page, M.T., Weiser, D.A., Goebel, T.H.W., and Hosseini, S.M.: Induced earthquake magnitudes are as large as (statistically) expected, Journal of Geophysical Research: Solid Earth, 121, (2016), 4575–4590, doi:10.1002/2016jb012818.

White, M.C.A., Ben-Zion, Y., and Vernon, F.L.: A Detailed Earthquake Catalog for the San Jacinto Fault-Zone Region in Southern California, Journal of Geophysical Research: Solid Earth, 124, (2019), 6908–6930, doi:10.1029/2019jb017641.

Zaliapin, I., and Ben-Zion, Y.: Earthquake Declustering Using the Nearest-Neighbor Approach in Space-Time-Magnitude Domain, Journal of Geophysical Research: Solid Earth, 125, (2020), doi:10.1029/2018jb017120.